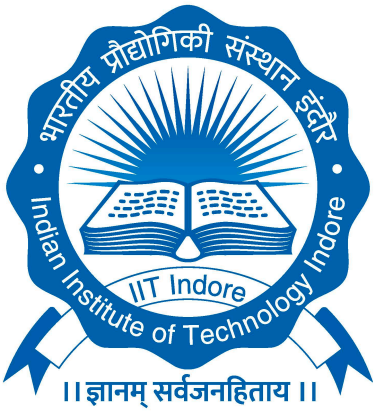
State Transitions in Accretion Discs induced by varying Mass Accretion Rate

M.Sc. Thesis

By
Sayan Maity



Department of Astronomy, Astrophysics and Space Engineering

INDIAN INSTITUTE OF TECHNOLOGY INDORE

May 8, 2026

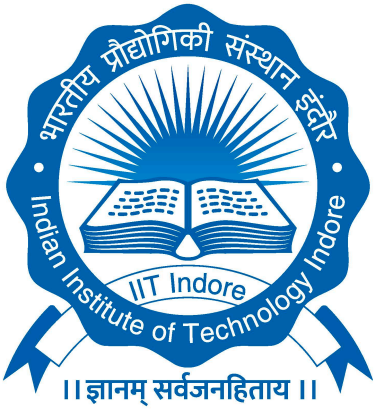
State Transitions in Accretion Discs induced by varying Mass Accretion Rate

A THESIS

Submitted in partial fulfillment of the requirements for the awards of the degree
of
Master of Science

By

Sayan Maity



Department of Astronomy, Astrophysics and Space Engineering

INDIAN INSTITUTE OF TECHNOLOGY INDORE

May 8, 2026

INDIAN INSTITUTE OF TECHNOLOGY INDORE

CANDIDATE'S DECLARATION

I hereby certify that the work which is being presented in the thesis entitled **State Transitions in Accretion Discs induced by varying mass accretion rate** in the partial fulfillment of the requirements for the award of the degree of **MASTER OF SCIENCE** and submitted in the **DEPARTMENT OF ASTRONOMY, ASTROPHYSICS AND SPACE ENGINEERING, Indian Institute of Technology Indore**, is an authentic record of my own work carried out during the time period from ----**June 2025**---- to ----**May 2026**---- under the supervision of **Dr. Ananda Deepika Bollimpalli**, **Assistant Professor, Department of Astronomy, Astrophysics and Space Engineering, IIT Indore.** The matter presented in this thesis has not been submitted by me for the award of any other degree of this or any other institute.

Sayan Maity
06/05/2026

Signature of the student with date
(SAYAN MAITY)

This is to certify that the above statement made by the candidate is correct to the best of my/our knowledge.

07-05-2026

Signature of the Supervisor of M.Sc. thesis (with date)
(Dr. ANANDA DEEPIKA BOLLIMPALLI)

SAYAN MAITY has successfully given his/her M.Sc. Oral Examination held on 05 May, 2026.

Signature(s) of Supervisor(s) of MSc thesis
Date: 07-05-2026

Programme Coordinator, M.Sc.
Date: 08/05/2026

Convener, DPGC
Date: 08/05/2026

HOD, DAASE
Date: 08/05/2026

Acknowledgements

I would like to express my sincere gratitude to my supervisor, Dr. Ananda Deepika Bollimpalli, for giving me the opportunity to work on this project and for her continual guidance throughout the course of this work. I would also like to thank Dr. Bhargav Vaidya for his useful insights regarding the PLUTO code. I am grateful to Mr. Devesh Sharma, PhD student at IIT Indore, for helping me with the entire setup and mechanism of the PLUTO code. I am also deeply thankful to my classmate and friend Sucharita for her support and for the many insightful discussions about my work.
Finally, I gratefully acknowledge the resources and facilities provided by the Discipline of Astronomy, Astrophysics and Space Engineering.

Abstract

State changes in accretion discs, particularly those observed during outbursts of X-ray binaries, remain poorly understood within the framework of disc evolution theory. Although observations consistently link these transitions to rapid variations in luminosity and spectral hardness, the underlying physical mechanism is still not well established.

In this work, we explore the role of optically thin radiative cooling in shaping radiatively inefficient accretion flows (RIAFs). When the cooling timescale exceeds the viscous timescale ($t_{\rm cool} \gtrsim t_{\rm visc}$), the flow maintains a geometrically thick structure and remains largely insensitive to changes in density or cooling efficiency. However, as the density increases, radiative cooling becomes efficient enough for the gas to lose energy before accretion, leading to the formation of a geometrically thin, optically thick disc.

For typical cooling processes such as bremsstrahlung, the flow naturally develops a two-component structure consisting of a hot inner flow and a cooler, thin outer disc. If the cooling timescale decreases further, the accretion flow separates into two distinct phases: a hot, radiatively inefficient coronal region and a cold, dense thin disc.

Our aim is to show that the transition from a quiescent hot RIAF state to a cold, blackbody-dominated disc is driven primarily by an increase in the mass accretion rate.

List of Figures

1.1 Equipotential contours (adapted from Fig 18.3 of Carroll & Ostlie [1]). 2
1.2 Roche geometry: R_1 and R_2 denote the radii of spheres whose volumes are equal to those of the respective Roche lobes(taken from[2]). 5

2.1 Pseudo color plot of density in the initial setup, i.e., at $t = 0$ 10

3.1 Pseudocolor density plot for an initial run with $\rho_0 = 10^6\, m_p$ g cm^{-3}. Fig (b) and (c) shows run without viscosity ie $\nu = 0$ and (d) and (e) shows run with viscosity ie $\nu \propto r^{1/2}$ as shown in equation 2.10. The grid resolution is 512 x 512 15
3.2 Mass accretion rate at $r = 100R_g$ over a range of 70° to 110°(mid plane region) throughout the runtime of 10 orbits in units of Solar Mass per year $M_\odot$ yr^{-1} . . 17
3.3 Outward Angular Momentum flux at $r = 100R_g$ over a range of 70° to 110°(mid plane region) throughout the runtime of 10 orbits 17
3.4 Pseudocolor density plot for an initial run with $\rho_0 = 10^6\, m_p$ g cm^{-3} with $R_0 = 100R_g$ and d = 1.3. The grid resolution is 512 x 512 18
3.5 Pesudocolor density plot for a run with $\rho_0 = 10^6\, m_p$ g cm^{-3} and cooling turned on, at t=350000(around 20 orbits). 19
3.6 Pesudocolor plots showing the ratio of cooling timescales to viscous timescales at t=350000(around 20 orbits). 19
3.7 The evolution of pseudocolor Temperature plots with time. $\rho_0 = 10^{10}\, m_p$ g cm^{-3}. The resolution of the run is 512 x 512 21
3.8 The variation of mid plane aspect ratio (H/R) with radius (r/R_g). The blue dotted lines and the orange line represent the plots corresponding to 3.5 orbits and 7 orbits respectively. 22
3.9 Pseudocolor density plot for cooling with $\rho_0 = 10^{10}\, m_p$ g cm^{-3} 22
3.10 The evolution of pseudocolor Temperature plots with time. $\rho_0 = 10^{10}\, m_p$ g cm^{-3}. The resolution of the run is 512 x 512 23
3.11 Transition from a geometrically thick RIAF state dominated by viscous heating into a geometrically thin cold disc induced by addition of mass. The grid reasolution is 512 x 512 25
3.12 High resolution run showing the transition from a hot RIAF state to a cold thin disc (around 8 orbits). 27
3.13 t_{cool}/t_{visc} ratio for high resolution run of state transition induced by an increase in mass accretion rate 28
3.14 The variation of mid plane aspect ratio (H/R) with radius (r/R_s). The blue dotted lines and the orange lines represent the plots corresponding to 0 and 8 orbits respectively. 28

Contents

Acknowledgments i

Abstract ii

1 Introduction 1
- 1.1 Binary Systems . . . 1
  - 1.1.1 Roche Lobe . . . 1
- 1.2 Accretion Disc . . . 3
  - 1.2.1 Disc Formation . . . 3
  - 1.2.2 Eddington Limit . . . 4
  - 1.2.3 Emitted Spectrum . . . 5
- 1.3 Black Hole Binaries . . . 6
  - 1.3.1 Spectral Characteristics . . . 6
  - 1.3.2 X-Ray States of Accretion Disc . . . 7
- 1.4 Problem . . . 7

2 Simulations of Radiatively Inefficient accretion flows and Optically Thin Radiative Cooling 8
- 2.1 Introduction . . . 8
- 2.2 Basic Hydrodynamic Equations . . . 9
- 2.3 Initial Setup . . . 10
- 2.4 Viscosity . . . 11
- 2.5 Numerical Setup . . . 12
- 2.6 Cooling . . . 12
- 2.7 Diagnostics . . . 13

3 Results and Discussion 14
- 3.1 Plots . . . 14
  - 3.1.1 Simulations without Cooling . . . 14
  - 3.1.2 Simulations with Cooling . . . 18
  - 3.1.3 State Transitions induced by cooling . . . 24

4 Future Work 29

Chapter 1

Introduction

1.1 Binary Systems

Stellar evolution usually ends with the formation of a compact star. A star during its lifetime is maintained by a hydrostatic equilibrium. The thermo-nuclear pressure generated in its core as a result of the fusion of atoms pushes outwards and counteracts the inward force of gravity. This is the invisible dance that keeps a star alive. However, as the material inside its core starts getting exhausted and there's not sufficient pressure to fuse higher elements, the outward pressure drops and gravity starts winning.

When this happens, the star collapses under its own weight. This will result in the formation of a very dense and compact stellar corpse, also known as a compact star. There are mainly three kinds of compact objects: White Dwarfs, Neutron Stars and Black Holes. Compactness is defined through the radius of the body relative to its gravitational radius

$$R \sim R_g = \frac{GM}{c^2}.$$

For white dwarfs, this is

$$\frac{R_g}{R} \sim 10^{-3} - 10^{-4},$$

so they are "weakly" compact.
For neutron stars,

$$\frac{R_g}{R} \sim 10^{-1},$$

so they are strongly compact

Compact objects such as white dwarfs, neutron stars, and black holes are often found in binary systems, where they orbit a companion star. If the companion star is very close, with a separation that is roughly equal to its diameter, then its outer layers are deformed into a teardrop shape. The distorted star may even lose some of its photospheric gases to its compact companion. The spilling of gas from one star onto another can lead to some spectacular firework, primarily called an **accretion disc**.

1.1.1 Roche Lobe

In a binary system, each star is surrounded by a region where its gravitational influence dominates. These regions are called **Roche lobes**, and their shape is determined by the combined

gravitational forces of both stars and the centrifugal effect in the rotating frame.

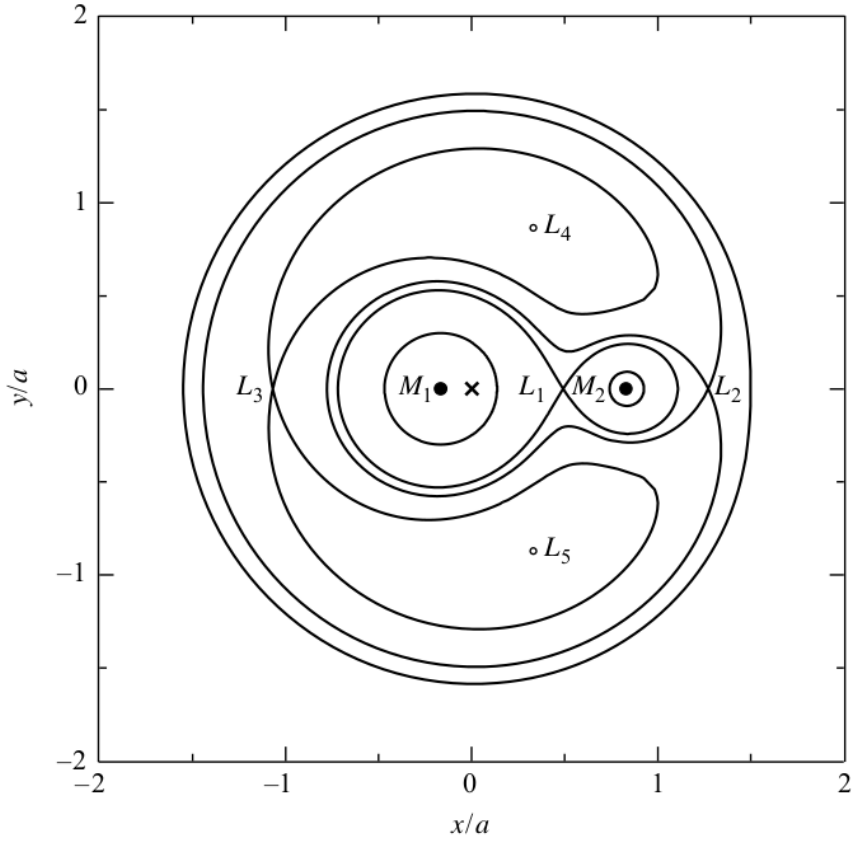


Figure 1.1: Equipotential contours (adapted from Fig 18.3 of Carroll & Ostlie [1]).

Consider two stars with masses M_1 and M_2 separated by a distance a. In a frame rotating with the binary, the effective potential experienced by a test particle of mass m in the orbital plane is [1]

$$\Phi = -G\left(\frac{M_1}{s_1} + \frac{M_2}{s_2}\right) - \frac{1}{2}\omega^2 r^2, \tag{1.1}$$

where s_1 and s_2 are the distances from the particle to each star, and ω is the orbital angular frequency. Equipotential surfaces of Φ define the Roche lobes. The inner Lagrangian point L_1 marks the location where the two lobes touch; mass can flow from one star to the other if a star expands beyond its Roche lobe.

Roche lobes are crucial in accreting systems because when a star fills its lobe, material can transfer to its companion, often forming an accretion disk around a compact object due to conservation of angular momentum. Approximate distances from L_1 to each star are given by [1]

$$\ell_1 = a\left(0.500 - 0.227\log_{10}\frac{M_2}{M_1}\right), \quad \ell_2 = a\left(0.500 + 0.227\log_{10}\frac{M_2}{M_1}\right). \tag{1.2}$$

Intuitively, Roche lobes set the boundary for possible mass transfer: if a star expands beyond its lobe, mass flows toward the companion, powering accretion and often producing an accretion disk. Fig 1.1 shows an eight-like contour: if one of the stars fills this area the matter can be stripped off from it and will flow to the other star through the L_1 point. The star that

loses materials is called the secondary star, and its companion is called the Primary/accretor.

1.2 Accretion Disc

During the nineteenth century, gravity was viewed as the only viable power source for astronomical objects, even though it could not account for the Sun's long lifetime. Today, however, gravitational energy plays the opposite role: it is recognized as the main driver behind some of the brightest phenomena in the Universe, far exceeding what nuclear fusion alone can produce. In many close binaries and in active galactic nuclei, the release of gravitational potential energy through accretion onto compact objects provides an extremely efficient mechanism for generating high-energy radiation. This modern picture has been reinforced by advances across the electromagnetic spectrum and by the confirmed existence of neutron stars and black holes.[2]

To see how powerful accretion can be, consider a mass M with radius R_*. The gravitational energy liberated when material of mass m settles onto its surface is

$$\Delta E_{\rm acc} = \frac{GMm}{R_*}. \tag{1.3}$$

For a neutron star with $M \sim M_\odot$ and $R_* \sim 10$ km, this corresponds to roughly 10^{20} erg per gram of accreted material, most of which is radiated electromagnetically.

By comparison, nuclear burning of hydrogen into helium releases

$$\Delta E_{\rm nuc} = 0.007mc^2, \tag{1.4}$$

or approximately 6×10^{18} erg g^{-1}. Thus, for neutron stars, accretion is nearly an order of magnitude more productive per unit mass than nuclear fusion.

The efficiency of accretion increases with the compactness M/R_*, making neutron stars and black holes particularly effective emitters. White dwarfs, with much larger radii, gain far less energy per unit mass through accretion than through nuclear burning. However, nuclear reactions on white dwarfs occur only during brief thermonuclear runaways (novae). For most of their evolution, accretion is their dominant radiative output. This is why cataclysmic variables—white dwarfs accreting from companion stars—serve as important laboratories for studying disk accretion. Accretion onto ordinary stars is much weaker, yet it remains astrophysically relevant in systems such as symbiotic stars.

For any compact object, the luminosity generated by accretion is set by the mass inflow rate $\dot{M}$. At sufficiently high luminosities, the radiation field exerts an outward force on the accreting gas, potentially limiting the inflow. This radiation–gravity balance leads to the Eddington luminosity, which defines the maximum steady luminosity an object of mass M can sustain.

1.2.1 Disc Formation

Mass transfer in close binaries often proceeds through Roche–lobe overflow, and the incoming material typically carries enough specific angular momentum to prevent it from falling directly onto the primary. As shown in Fig. 1.4, gas leaving the secondary crosses the L_1 point and enters the primary's Roche lobe. To the primary, this stream resembles matter emerging from a rapidly rotating nozzle. Except in systems with very long orbital periods, the L_1 region moves so quickly that the flow approaches the primary nearly perpendicular to the line joining the two stars.[2]

A good approximation is to treat the gas as a test particle released from L_1 with a fixed specific angular momentum and then allowed to move in the gravitational potential of the primary. Because the equipotentials inside each Roche lobe are nearly circular, the trajectory is close to an elliptical orbit in the orbital plane. The secondary's gravity produces only a slow precession, since the potential deviates from the pure $1/r$ form of a Kepler problem.

A continuous gas stream cannot follow this path without intersecting itself, generating shocks and losing energy. However, the material retains most of its angular momentum, so it naturally settles onto the lowest-energy orbit compatible with that angular momentum: a circular orbit. The radius of this orbit, $R_{\rm circ}$, is defined such that a Keplerian orbit there has the same specific angular momentum as matter at L_1. The corresponding orbital speed is

$$v_\phi(R_{\rm circ}) = \left(\frac{GM_1}{R_{\rm circ}}\right)^{1/2}. \tag{1.5}$$

Typically, the circularization radius $R_{\rm circ}$ is a few times smaller than the primary's Roche-lobe radius R_L. Thus, unless the primary has a physical radius larger than $R_{\rm circ}$, the transferred gas remains well inside its Roche lobe. For neutron stars, black holes, and most compact objects, $R_* < R_{\rm circ}$ is always satisfied.

This difference between R_* and $R_{\rm circ}$ has important consequences. Rather than forming a single particle orbit, the steady inflow from the secondary collects into a ring of gas at $R_{\rm circ}$. Dissipative effects—shocks, collisions, viscosity, and magnetohydrodynamic turbulence [3]—convert orbital kinetic energy into heat, which is radiated away.

Because the gas loses energy more efficiently than angular momentum, it drifts inward into regions of deeper gravitational potential. A circular orbit minimizes the energy for a fixed angular momentum, so the material settles into a series of nearly circular orbits, producing an accretion disc. Angular momentum must be transported outward for this inflow to occur, causing the outer disc to gain angular momentum and expand. Consequently, the initial ring spreads both inward and outward.

A key implication is that the outer radius of the disc, $R_{\rm out}$, is generally larger than the circularization radius $R_{\rm circ}$. For this reason, $R_{\rm circ}$ is considered the minimum possible disc size. The disc cannot grow without limit, however; its outer edge must remain inside the primary's Roche lobe.

1.2.2 Eddington Limit

A simple estimate of radiation–gravity balance can be obtained by considering steady, spherically symmetric accretion. Assume the inflowing gas is hydrogen-rich and fully ionized, so photons primarily interact with free electrons through Thomson scattering; proton scattering is negligible because its cross-section is smaller by a factor of $(m_e/m_p)^2 \approx 5 \times 10^{-4}$.[2]

If the radiative flux is S (erg s^{-1} cm^{-2}), each electron experiences an outward force $\sigma_T S/c$, where $\sigma_T = 6.7 \times 10^{-25}$ cm^2 is the Thomson cross-section. Electrons and protons are tightly coupled through Coulomb forces, so radiation pushes entire electron–proton pairs outward. Meanwhile, gravity exerts an inward force of $\approx GMm_p/r^2$ on each pair.

For a luminosity L, spherical symmetry gives $S = L/(4\pi r^2)$, so the net radial force is

$$GMm_p - \frac{L\sigma_T}{4\pi c}. \tag{1.6}$$

Setting this equal to zero defines the Eddington luminosity,

$$L_{\rm Edd} = \frac{4\pi GMm_p c}{\sigma_T} \approx 1.3 \times 10^{38}\,(M/M_\odot)\ \text{erg s}^{-1}. \tag{1.7}$$

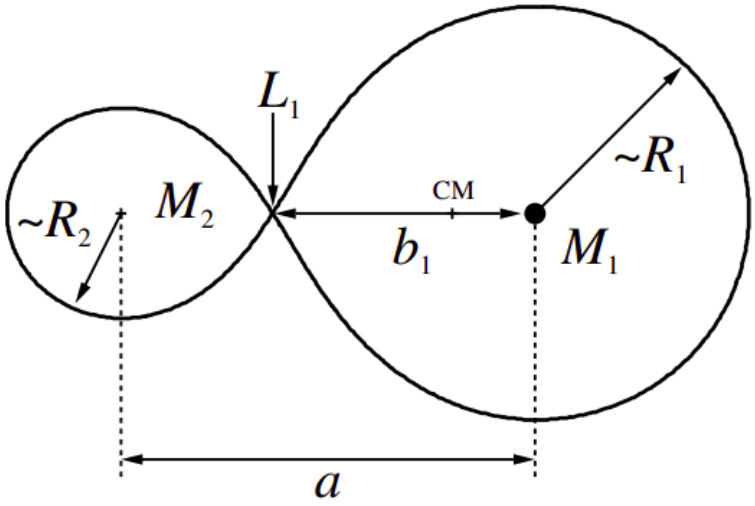


Figure 1.2: Roche geometry: R_1 and R_2 denote the radii of spheres whose volumes are equal to those of the respective Roche lobes(taken from[2]).

If a source radiates above this limit, radiation pressure overwhelms gravity: accretion is halted if luminosity is accretion-powered, or outer layers are expelled if nuclear burning dominates. A similar argument yields the maximum stable stellar mass.

The usefulness of L_{Edd} depends on the assumptions that entered its derivation: steady flow, spherical symmetry, and fully ionized hydrogen. If only a fraction f of the surface accretes, the limit increases to fL_{Edd}, while complex geometries weaken the predictive power of the simple estimate. The steady-flow requirement is particularly restrictive—supernovae, for instance, easily exceed L_{Edd}. Although heavy elements can modify the opacity, strong X-ray fields often maintain full ionization.

Despite these simplifications, the Eddington limit remains a valuable diagnostic, especially for systems radiating near this value. For accretion-powered sources, it also sets the maximum steady mass inflow rate. If the gravitational energy of the infalling gas is fully radiated at the stellar surface R_*, the accretion luminosity is

$$L_{\text{acc}} = \frac{GM\dot{M}}{R_*}. \tag{1.8}$$

1.2.3 Emitted Spectrum

Simple estimates of characteristic photon energies can help identify the nature of an accreting compact object. A convenient description uses a radiation temperature T_{rad}, defined so that a typical photon energy $h\bar{\nu}$ satisfies $h\bar{\nu} \sim kT_{\text{rad}}$; the exact choice of $\bar{\nu}$ is unimportant for order-of-magnitude arguments.[2]

For an object of radius R_* radiating with luminosity L_{acc}, we introduce a blackbody temperature

$$T_b = \left(\frac{L_{\text{acc}}}{4\pi R_*^2 \sigma}\right)^{1/4},$$

the temperature the surface would have if the emission were purely blackbody.

A second scale is the thermal temperature $T_{\rm th}$, obtained by equating the gravitational energy released by a proton–electron pair, GMm_p/R_*, with its thermal energy $3kT$:

$$T_{\rm th} = \frac{GMm_p}{3kR_*}. \tag{1.9}$$

If the accreting gas is optically thick, the radiation is thermalized before escaping and $T_{\rm rad} \approx T_b$. If the gas is optically thin—such as in strong-shock regions—the energy is emitted immediately, and $T_{\rm rad}$ instead approaches $T_{\rm th}$.

Thus the characteristic photon temperature typically lies between these two limits,

$$T_b \lesssim T_{\rm rad} \lesssim T_{\rm th}.$$

Accretion flows around compact objects often reach temperatures high enough to emit primarily in X-rays, which is why such systems are collectively known as **X-ray Binaries (XRBs)**.

1.3 Black Hole Binaries

In a landmark contribution, Oppenheimer and Snyder (1939) provided the first fully theoretical framework describing how black holes can form. Decades later, compelling observational support for such objects emerged from X-ray and optical studies of the binary system Cygnus X–1 [4]. Modern X-ray observations of black-hole binaries (BHBs) have become essential for probing both black hole properties and the physics of accretion. At present, roughly twenty known X-ray binaries contain compact objects whose inferred masses exceed the maximum allowed for neutron stars or other degenerate remnants (i.e., $M > 3\,M_\odot$), and are therefore classified as BHBs.

One of the most informative diagnostics of the immediate environment around a black hole is the rapid, short-timescale variability frequently seen in their X-ray emission. Such fast fluctuations are typically analyzed using power-density spectra, which reveal the temporal structure of the signal. BHBs commonly undergo outbursts in which their X-ray luminosity rises sharply and then gradually declines over periods of weeks to months. Because nearly all BHBs are first detected when they enter such high-intensity states, their discovery and continued monitoring rely heavily on wide-field X-ray instruments aboard satellites. Light curves from different systems display a remarkable variety of shapes, reflecting a wide range of rise and decay timescales across the BHB population.

1.3.1 Spectral Characteristics

It has been understood for many years that the X-ray spectra of black-hole binaries (BHBs) typically contain two distinct components: a thermal part and a nonthermal one. These systems also undergo spectral state transitions during which one of these components can become the dominant contributor to the X-ray output [5]. The thermal emission arises from the inner regions of the accretion disk and is well described by a multitemperature blackbody spectrum, usually characterized by temperatures on the order of 1 keV. The nonthermal component is generally represented by a power-law (PL) distribution with photon index Γ, so that the photon number spectrum scales as $N(E) \propto E^{-\Gamma}$. This PL component reaches substantially higher photon energies than the disk emission and often shows either a high-energy cutoff or a spectral

break.

1.3.2 X-Ray States of Accretion Disc

The concept of distinct X-ray states emerged after Tananbaum et al. (1972)[6] documented a dramatic spectral change in Cyg X–1: the soft X-ray flux in the 2–6 keV band dropped by a factor of four, while the hard 10–20 keV flux increased by roughly a factor of two, accompanied by the appearance of radio emission.

The *soft state* is dominated by thermal disk emission with characteristic temperatures around ~ 1 keV, and it is typically associated with higher luminosities, which led to its designation as the "high/soft state."

By contrast, the *hard state* features a power-law spectrum with photon index $\Gamma \sim 1.7$ and is usually observed when the system is fainter, hence the term "low/hard state." In this regime, the accretion disk is either absent above 2 keV or appears much cooler and shifted to larger radii from the black hole.

There are quite a few intermediate states a system can undergo through but it can broadly be classified into to distinct states:

1. Radiatively inefficient accretion flows (RIAFs): optically thin, geometrically thick, hot flows that are poor radiators.[7]

2. Shakura–Sunyaev thin discs: optically thick, geometrically thin, cool flows that radiate efficiently as a multi-temperature blackbody.[8]

1.4 Problem

X-ray binaries (XRBs) often undergo transitions between these states, producing observable spectral changes. The physical mechanism underlying these transitions is a key open problem in high-energy astrophysics.

Previous work [9] has shown through simulations that a transition from high to soft state can be triggered when the cooling timescale becomes shorter than the viscous timescale, typically achieved by an increase in the mass accretion rate. Conversely with low accretion rate the thin disc(soft) can transition into a RIAF(hard). However, the physical origin of this increase is not properly understood.

In this work, we revisit the problem of accretion state transitions through simulations with the `PLUTO` code [10].

Chapter 2

Simulations of Radiatively Inefficient accretion flows and Optically Thin Radiative Cooling

2.1 Introduction

Astrophysical black holes (BHs) are generally divided into two main populations: stellar-mass BHs ($\sim 10\,M_\odot$), which are formed as the endpoints of massive stellar evolution [11], and supermassive BHs ($\sim 10^6$–$10^{10}\,M_\odot$) located at the centres of galaxies. These systems typically exhibit two distinct accretion regimes.

The first regime corresponds to a hot, geometrically thick, and optically thin flow that is radiatively inefficient (e.g. [7, 12]). The second regime is a cool, geometrically thin, and optically thick disc that emits approximately as a blackbody [8]. High-redshift quasars, which show strong thermal emission, are interpreted as systems undergoing thin-disc accretion onto supermassive BHs. By contrast, low-luminosity AGN in the local Universe, which lack significant thermal signatures, are well described by radiatively inefficient accretion flow (RIAF) models.

In X-ray binaries (XRBs), the shorter characteristic timescales enable the same system to switch between these accretion states, evolving from a quiescent RIAF phase to a thermally dominated, blackbody-emitting state and back again (see [5] for a review).

In most numerical studies, the RIAF regime is modelled without explicitly including radiative cooling or detailed radiation transport, as these effects are typically subdominant (e.g. [13, 14, 15, 16]). In contrast, simulations of thin discs are significantly more challenging due to their extremely small aspect ratio ($H/R \sim 10^{-3}$–10^{-2}), which demands very high spatial resolution.

Although significant progress has been made in incorporating additional physics such as cooling, radiation, and magnetic fields (e.g. [17, 18]), a fully self-consistent treatment of all relevant processes across all regimes remains computationally prohibitive.

In this work, we perform hydrodynamic simulations of accretion flows using a prescribed viscous model. Our goal is to investigate the impact of bremsstrahlung cooling on the global structure of the flow.

While angular momentum transport in accretion discs is widely attributed to magnetohydrodynamic (MHD) turbulence driven by the magnetorotational instability (e.g. [3]), we instead adopt a phenomenological viscosity prescription. This simplifies the problem by avoiding the complexities of full MHD simulations, allowing us to focus on the combined effects of viscous

transport and radiative cooling. Within this framework, we examine how varying physical parameters influence the emergence of a hot, diffuse corona and a cool, geometrically thin disc [9].

We find that the formation of a thin disc at a given radius occurs when the ratio $t_{\rm cool}/t_{\rm visc} \ll 1$ at that location, consistent with earlier expectations [12]. From our idealised simulations, we identify the physical processes responsible for state transitions in accretion flows and demonstrate that an increase in the mass accretion rate can drive the system from a low-hard (RIAF) state to a high-soft (thin-disc) state.

The following section describes the numerical methods employed, followed by a discussion of the results.

2.2 Basic Hydrodynamic Equations

We solve the fundamental hydrodynamic equations in spherical polar coordinates (r, θ, ϕ) using the `PLUTO` code. The governing equations are as follows:[9]

Continuity equation:

$$\frac{d\rho}{dt} + \rho\,\nabla \cdot \mathbf{v} = 0, \tag{2.1}$$

Momentum equation:

$$\frac{d\mathbf{v}}{dt} = -\nabla P - \rho\,\nabla\phi + \nabla \cdot \boldsymbol{\sigma}, \tag{2.2}$$

Energy equation:

$$\rho\,\frac{d}{dt}\left(\frac{e}{\rho}\right) = -P\,\nabla \cdot \mathbf{v} + \frac{\sigma^2}{\mu} - n_e n_i \Lambda(T). \tag{2.3}$$

In the present formulation, ρ represents the mass density, P the gas pressure, and $\mathbf{v} = (v_r, v_\theta, v_\phi)$ denotes the velocity field. The internal energy density is given by e, for which we adopt $e = 3P/2$, consistent with an ideal gas having adiabatic index $\gamma = 5/3$. This assumption is justified since the ions remain non-relativistic except in the immediate vicinity of the black hole.

The dynamic viscosity is expressed as $\mu = \nu\rho$, where ν is the kinematic viscosity coefficient, and $\boldsymbol{\sigma}$ denotes the viscous stress tensor. The electron and ion number densities are written as n_e and n_i, respectively, while $\Lambda(T)$ represents the temperature-dependent radiative cooling function. The Lagrangian (or material) derivative is defined as

$$\frac{d}{dt} = \frac{\partial}{\partial t} + \mathbf{v} \cdot \nabla.$$

[9]

For the gravitational potential of the central black hole, we use simple newtonian potential,

$$\phi = -\frac{GM}{r}, \tag{2.4}$$

where M is the black hole mass, G the gravitational constant, c the speed of light, and r is the spherical radius.

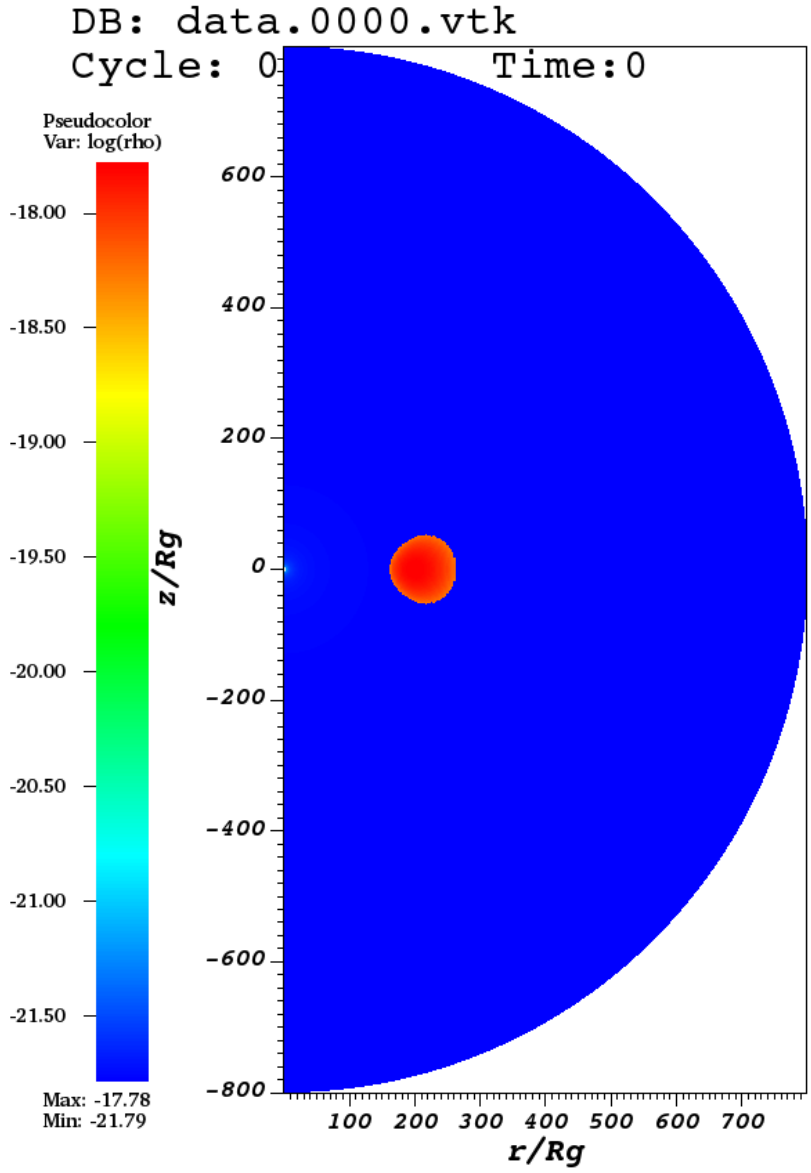


Figure 2.1: Pseudo color plot of density in the initial setup, i.e., at $t = 0$

2.3 Initial Setup

Our simulations begin with a dense torus in dynamical equilibrium, characterized by a constant specific angular momentum a shown in Fig 2.1. This torus is surrounded by a non-rotating background medium of very low density. Within the torus, the pressure and density obey a polytropic relation,

$$P = K\rho^{\gamma},$$

where K is a constant. Following the procedures of [19] and [13], the initial torus configuration for our gravitational potential ϕ is given by[9]

$$\frac{P}{\rho} = \frac{GM}{(n+1)R_0}\left[\frac{R_0}{r} - \frac{R_0^2}{2R^2} - \frac{1}{2d}\right], \tag{2.5}$$

where $R = r\sin\theta$ denotes the cylindrical radius, R_0 is the equatorial location of the torus center (where the density is maximum), and $d > 1$ is a distortion parameter that controls the shape and thickness of the torus. When $d \approx 1$, the cross-section is nearly circular and compact; for much larger values of d, the torus becomes broader and more distorted. The polytropic index is $n = 1/(\gamma - 1)$. In most of our simulations, we adopt $d = 1.125$.

At the torus center ($r = R_0$, $\theta = 90°$), the density reaches its maximum value ρ_0($\rho_0 = 10^6\, m_{\rm p}$ g cm^{-3}). Using this condition, the constant K can be expressed as

$$K = \frac{GM}{(n+1)R_0\rho_0^{\gamma-1}}\left[\frac{1}{2} - \frac{1}{2d}\right]. \tag{2.6}$$

Thus, once ρ_0 and d are specified, the value of K follows directly.

The ambient medium surrounding the torus is kept in an isothermal state with a low density profile of

$$\rho_a(r) = \eta\rho_0 \exp\left[\frac{GM}{a^2}\left(\frac{1}{r} - \frac{1}{r_{\rm min}}\right)\right] \tag{2.7}$$

where $\eta = 10^{-4}$ and $r_{\rm min}$ is the inner boundary of the torus, ensuring that it does not influence the torus dynamics. We adopt a black hole mass corresponding to Sgr A*, [20].

In the absence of radiative cooling, Eqs. (2.1)–(2.3) are invariant under a rescaling of the density normalization. This arises because both the pressure and viscous stress depend linearly on density, with $P \propto \rho$ and $\boldsymbol{\sigma} \propto \mu \propto \rho$, provided that the kinematic viscosity ν is independent of density. Consequently, the global structure of the accretion flow does not change when the density is rescaled by its initial peak value. This scaling invariance is also reflected in numerical simulations, where flows starting from different initial densities evolve toward comparable configurations at late times.

Furthermore, when all spatial coordinates are expressed in units of the gravitational radius R_g, velocities are scaled by the speed of light c, and densities are normalised with respect to the initial maximum value ρ_0, Eqs. (2.1)–(2.7) become independent of the black hole mass in the absence of cooling. The remaining physical variables are subsequently normalised within the `PLUTO` framework. As a result, the simulations are scale-free and applicable across a wide range of systems, from stellar-mass black holes in X-ray binaries to supermassive black holes in active galactic nuclei.

2.4 Viscosity

The term on the right-hand side of equation (2.3) accounts for heating arising from viscous dissipation. Results from MHD simulations (e.g., Brandenburg et al. 21; see table 2 in Hawley et al. 22) indicate that the $r\phi$ component of the magnetic stress dominates the stress tensor. Although magnetic fields are not included in the present study, we approximate their effect by assuming that only the $r\phi$ component of the viscous stress tensor $\boldsymbol{\sigma}$ is non-zero: [9]

$$\sigma_{r\phi} = \sigma_{\phi r} = \mu r\frac{\partial}{\partial r}\left(\frac{v_\phi}{r}\right). \tag{2.8}$$

For our simulations, the fiducial kinematic viscosity is chosen to follow

$$\nu \propto r^{1/2},$$

in accordance with theoretical expectations. In the conventional thin disc 'α-disc' framework, the viscosity is expressed as

$$\nu = \alpha c_s H, \tag{2.9}$$

where α is the Shakura–Sunyaev parameter, c_s the sound speed, and H the disc scale height [8].

Since $H \sim c_s/\Omega$, with Ω denoting the angular velocity, we obtain[9]

$$\nu \approx \alpha H^2 \approx \alpha \left(\frac{H}{r}\right)^2 r^2.$$

For Keplerian rotation, $\Omega \propto r^{-3/2}$, implying that

$$\nu \propto r^{1/2},$$

as long as H/r remains constant, which holds for a Shakura–Sunyaev disc.

The fiducial kinematic viscosity is then given by[9]

$$\nu = 4.5 \times 10^{-4}\, \Omega_0\, R_0^2 \left(\frac{\alpha}{0.01}\right) \left(\frac{r}{R_0}\right)^{1/2}. \tag{2.10}$$

[9]

2.5 Numerical Setup

We carry out two-dimensional axisymmetric hydrodynamic simulations in spherical coordinates (r, θ, ϕ). The computational domain extends from an inner boundary at $R_{\text{min}} = 3.5\, R_g$ to an outer boundary at $R_{\text{max}} = 800\, R_g$. A logarithmically spaced grid is used in the radial direction to better resolve the inner regions, while the polar angle θ is discretized uniformly over the full range $0 \leq \theta \leq \pi$. Although the system is axisymmetric and therefore independent of ϕ, the azimuthal coordinate is formally retained over $0 \leq \phi \leq 2\pi$.

At the inner radial boundary, we apply an inflow condition that allows matter to accrete into the black hole while preventing any outward flux. At the outer boundary, an outflow condition is imposed so that material can leave the computational domain freely, but no inflow from outside is permitted [9].

The standard resolution adopted in most runs is $N_r = N_\theta = 512$, where N_r and N_θ denote the number of grid cells in the radial and polar directions, respectively. For computationally inexpensive test runs, such as those executed on a laptop, we use a reduced resolution of $N_r = N_\theta = 128$.

2.6 Cooling

A bremsstrahlung cooling term is incorporated into the energy equation (the last term on the right-hand side of equation (3)). For this, we adopt the cooling function $\Lambda(T)$ from equation (12) of Sharma et al. [23], which is based on Sutherland and Dopita [24] and assumes mean molecular weights of $\mu = 0.62$ and $\mu_e = 1.18$. [9]

In this study, we do not account for cooling from synchrotron or inverse Compton processes. Although these mechanisms can be significant in certain accretion regimes, they are challenging to model accurately. Both synchrotron and Compton cooling are expected to scale as n^2, where n is the particle number density, since the magnetic and radiation energy densities generally track the mass accretion rate. Consequently, their inclusion would likely produce results that are qualitatively similar to those obtained with bremsstrahlung cooling.

2.7 Diagnostics

We consider three key characteristic timescales in the system [9]:

- The radiative cooling time, $t_{\rm cool} \propto 1/n$,
- The viscous timescale, $t_{\rm visc} = r^2/\nu$,
- The dynamical (free-fall) timescale, $t_{\rm ff} = \sqrt{2r^3/GM}$.

In radiatively inefficient accretion flows (RIAFs), when the cooling timescale becomes significantly shorter than the viscous timescale ($t_{\rm cool} \ll t_{\rm visc}$), the flow naturally bifurcates into two components. One component is a hot, dilute coronal region characterised by long cooling times, while the other is a cold, dense, geometrically thin, and optically thick disc. Each phase maintains thermal balance independently: in the thin disc, viscous dissipation is radiated away efficiently as blackbody emission, whereas in the corona, viscous heating is primarily balanced by optically thin radiative losses and adiabatic expansion [9].

Such a two-phase configuration emerges because a uniformly optically thin, strongly cooling accretion flow is inherently thermally unstable (e.g., [25]). By contrast, the combined corona–disc system achieves global stability. When radiative cooling in the corona exceeds local heating, excess material condenses onto the thin disc, restoring equilibrium. If heating dominates instead, part of the disc material is evaporated into the corona and can also contribute to outflows [9].

Despite this global balance, the corona can still exhibit local thermal instability in regimes where cooling is efficient. In such cases, small perturbations may lead to the formation of cold, dense clumps that condense out of the hot phase and accrete onto the thin disc [26].

Chapter 3

Results and Discussion

3.1 Plots

In addition to runs with cooling we also discuss some runs without cooling to discuss pure RIAF state ([13],[14],[27]). We then implement the external mass source function given in Equation 13 of [9] to study its effects on accretion flow. We discuss the results obtained and try to model an accretion flow and the procceses behind it.

3.1.1 Simulations without Cooling

We analyse pseudo color density plots for different conditions. As we turn off cooling (drop the last term of equation 2.3), we wish to produce a pure Radiatively Inefficient Accretion Flow (RIAF) state. For our runs the maximum density is defined as $\rho_0 = 10^6\, m_p$ g cm^{-3} at a distance R_0= 200 R_g. The density profile is motivated from the observations of $SgrA^{\star}$.[28] The torus is evolved for around 10 orbits so that it reaches a steady state. As viscosity is responsible for the accretion of matter, without viscosity the torus should retain its initial structure and not evolve as we see in Fig 3.1(c). Only at later time does a thin envelop of density appear around the torus due to a slight shift in equilibrium[9].
With

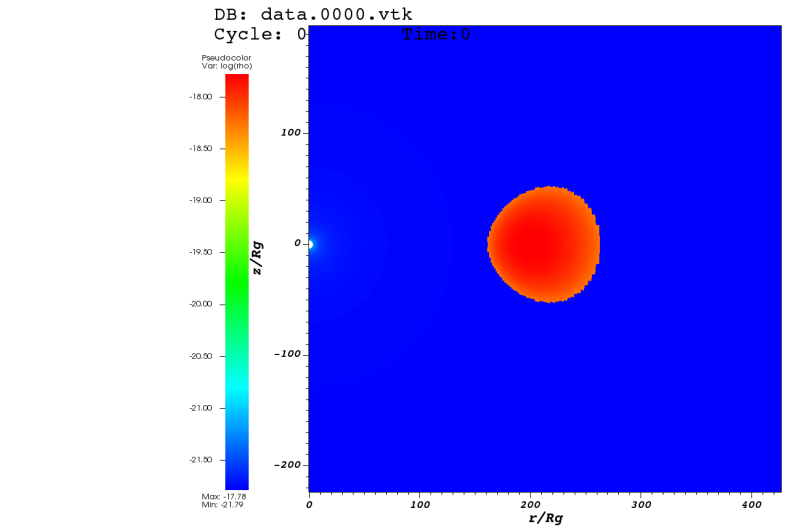
$$\nu \propto r^{1/2},$$

we see matter starting to accrete and enter a pure RIAF state as seen in 3.1(e). A geometrically thick RIAF is formed in the inner region while the matter in the outer region tapers into a tail-like structure because some matter has to be transported outward to allow matters to accrete. This phenomenon is known as angular momentum transport, where the angular momentum is transported outward in the accretion flow to allow matter to fall. The inner bulge constitutes of the corona (we use corona to describe the hot part of the flow where $t_{cool} > t_{visc}$). Note that the low density corona develops due to the accretion of matter and should not be confused with the low density ambient medium present for numerical purposes.[9] The density values are in g cm^{-3} plotted on a log scale.

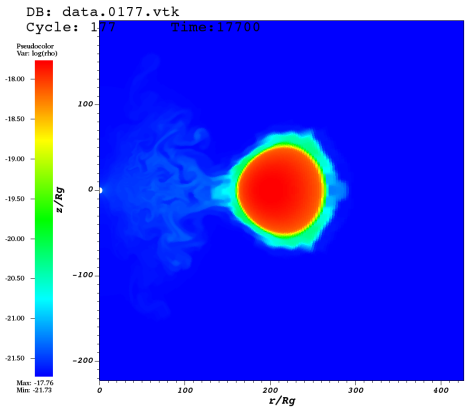
If we plot the mass accretion rate at a point $r = 100R_g$ over a range of theta from 70° to 110° (to focus mainly near the mid plane region)

$$\dot{M}(r) = \oint \rho\, \mathbf{v} \cdot d\mathbf{S} = \int_0^{2\pi} \int_0^{\pi} \rho(r,\theta,\phi)\, v_r(r,\theta,\phi)\, r^2 \sin\theta\, d\theta\, d\phi. \tag{3.1}$$

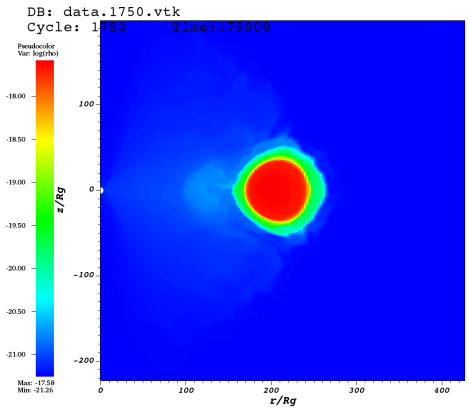
for the run without viscosity we see small fluctuations in the mass accretion rate in the initial phases due to small pressure gradients, which very soon stabilizes around 0 to signify no matter



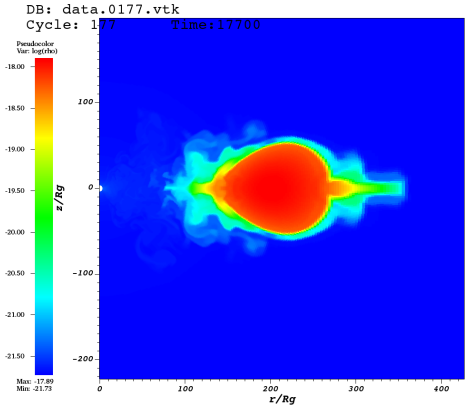
(a) t = 0



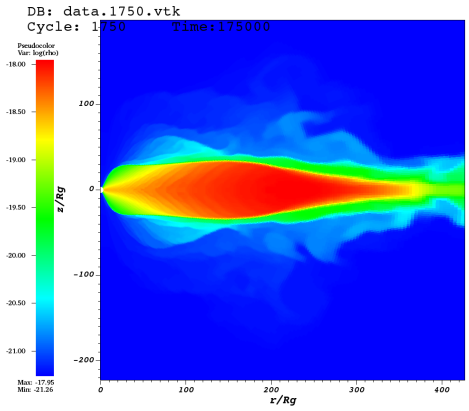
(b) 1 orb



(c) 10 orbs



(d) 1 orb



(e) 10 orbs

Figure 3.1: Pseudocolor density plot for an initial run with $\rho_0 = 10^6\, m_p\, \mathrm{g\ cm^{-3}}$. Fig (b) and (c) shows run without viscosity ie $\nu = 0$ and (d) and (e) shows run with viscosity ie $\nu \propto r^{1/2}$ as shown in equation 2.10. The grid resolution is 512 x 512

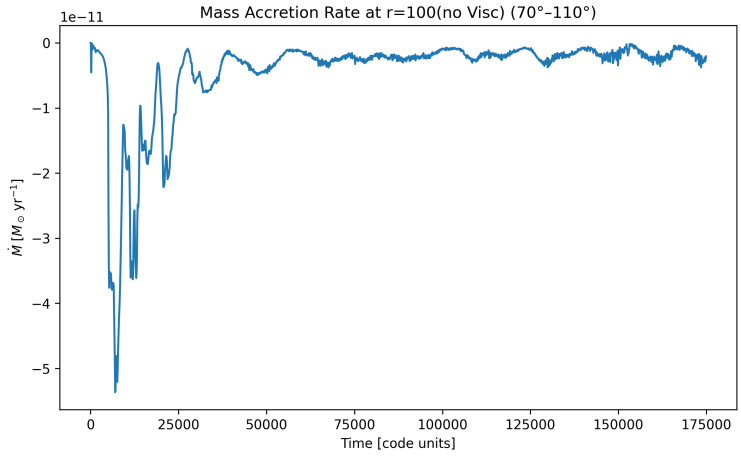
is being accreted and the torus enters a steady state in equilibrium(as shown in Figure 3.2(a). Consequently for the run with viscosity there is a significant fluctuation in the mass accretion rate with the average plummeting down to a negative value(Fig 3.2(b)). The negative mass

accretion rate is just a matter of convention that arises by treating the radial velocities inwards as negative and consequently an outward flow is considered positive.
If we further want to visualize the outward flow of matter through angular momentum transport we can plot radial outward angular momentum flux given by the expression

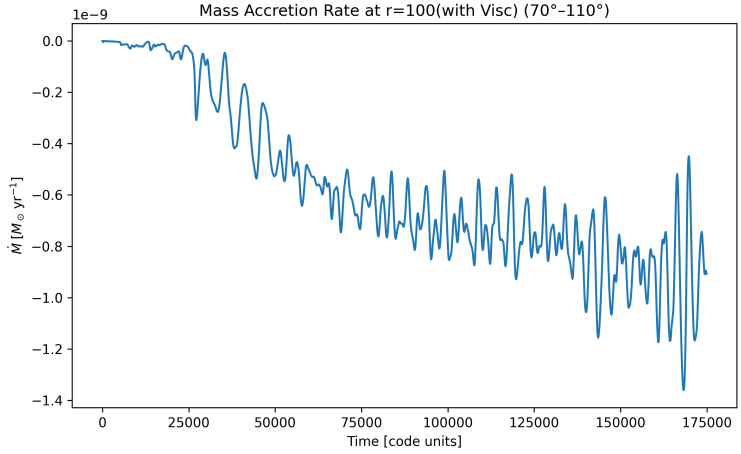
$$\dot{L}(t) = 2\pi r^3 \int_{\theta_1}^{\theta_2} \rho\, v_r\, v_\phi\, \sin^2\theta\, d\theta$$

at r = $100R_g$ as shown in Fig 3.3. Note in this case we only consider radial velocities with positive values (outward flow). We see for the no viscosity run after some initial fluctuations the value oscillates around 0 while for our viscosity run we see an average increase in the outward angular momentum showing mass is being transported outward allowing matter to accrete.

In the simulation physical quantities like length, velocity, density and time are defined by code units. The gravitational radius of the Black hole and the speed of light are set to unity in our code. Which makes the value of GM/c^3 = 1. t=177 refers to the value of $177GM/c^3$ and so on.

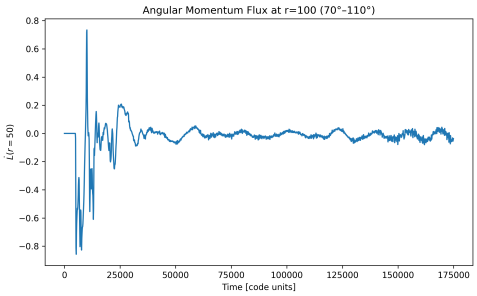


(a) No Viscosity $\nu = 0$

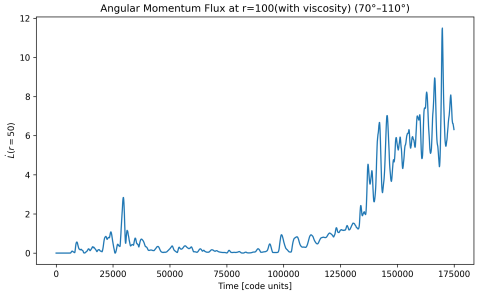


(b) With viscosity$\nu \propto r^{1/2}$

Figure 3.2: Mass accretion rate at $r = 100R_g$ over a range of 70° to 110°(mid plane region) throughout the runtime of 10 orbits in units of Solar Mass per year $M_\odot$ yr^{-1}



(a) No Viscosity $\nu = 0$



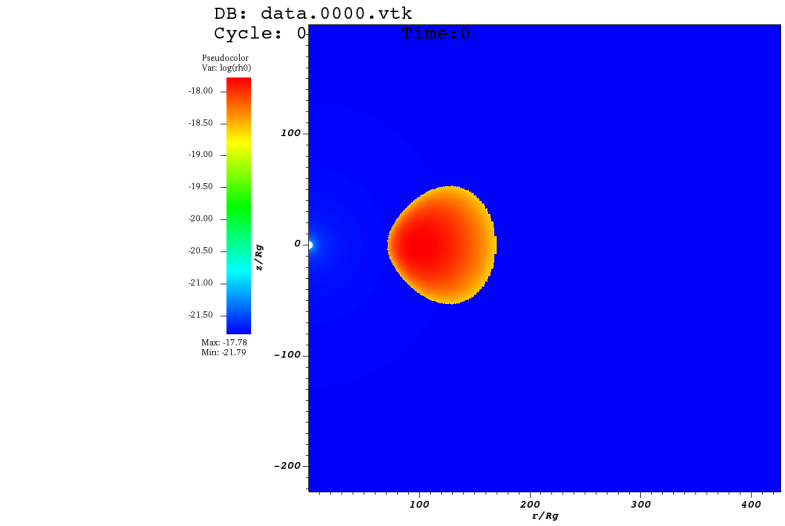
(b) With viscosity$\nu \propto r^{1/2}$

Figure 3.3: Outward Angular Momentum flux at $r = 100R_g$ over a range of 70° to 110°(mid plane region) throughout the runtime of 10 orbits

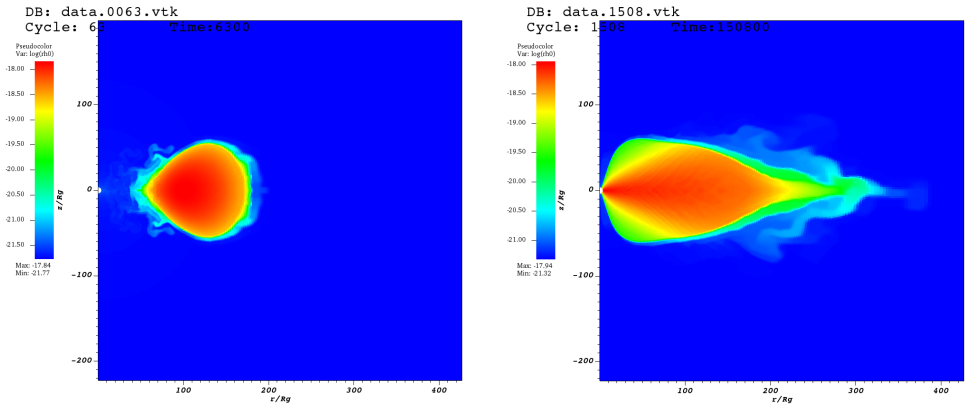
Dependence on varying parameters

In order to find out how sensitive our torus and its development is over our initial conditions we carry out a few test runs. First, the initial torus was positioned at a different radial distances

from the black hole, specifically at $R_0 = 100R_g$ (with $d = 1.125$ and $\nu \propto r^{1/2}$). In this case, the steady-state density contours in the inner accretion region were found to be nearly identical in structure to our original run. We then changed the initial cross-sectional size of the torus. The case considered was $d = 1.3$, corresponding to a thicker torus with a more distorted cross section (with $R_0 = 100\, R_g$ and $\nu \propto r^{1/2}$) [9]. Once again, the resulting inner steady-state density distribution was very similar to our original run (as shown in Fig 3.4).
These findings suggest that the final steady state is largely insensitive to the initial setup. In particular, the accretion flow does not strongly depend on the initial matter distribution or the specific manner in which the black hole is supplied with material, provided that the circularization radius (R_0) is sufficiently larger than the Schwarzschild radius.



(a) t = 0



(b) 1 orb **(c)** 24 orbs

Figure 3.4: Pseudocolor density plot for an initial run with $\rho_0 = 10^6\, m_p$ g cm^{-3} with $R_0 = 100R_g$ and d = 1.3. The grid resolution is 512 x 512

3.1.2 Simulations with Cooling

Here we discuss the effects of Bremsstrahlung cooling on accretion flows. In the absence of cooling the simulations are invariant to the density normalization as discussed before. However in the presence of cooling we should not expect the same as the cooling function scales with density as $\propto \rho^2$. Runs with low density remain an RIAF throughout; however we find a density

threshold above which the hot gas condenses and we see a transition into a thin disc. Though normally $\dot{M}$ woulld be a suitable parameter to study this transition but in our case ρ_o provides as a appropriate proxy.

We initialize our same density run as before with $\rho_0 = 10^6\, m_p$ g cm^{-3} with the cooling turned on since t=0 and evolve it for around 20 orbits. Even with such longer timescales the simulation remains a RIAF throughout, suggesting enough density is not yet reached to transition as shown in Fig 3.5. As $t_{cool} \propto 1/\rho$ the low density ensures that cooling timescales never becomes less than the viscous timescales thus never allowing the gas to cool. As we see in Fig 3.6 even in the central regions $t_{cool}/t_{visc} \sim 100$, suggesting the gas accretes much before it can cool.

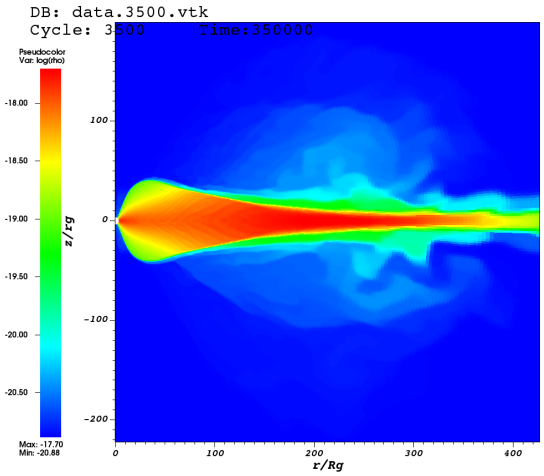


Figure 3.5: Pesudocolor density plot for a run with $\rho_0 = 10^6\, m_p$ g cm^{-3} and cooling turned on, at t=350000(around 20 orbits).

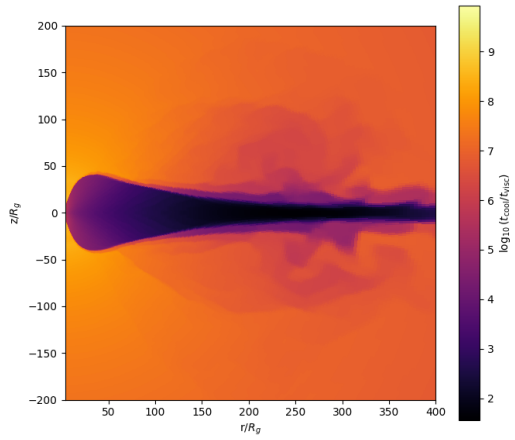


Figure 3.6: Pesudocolor plots showing the ratio of cooling timescales to viscous timescales at t=350000(around 20 orbits).

We next present results from a simulation with $\rho_0 = 10^{10}\, m_p$ g cm^{-3} and $\alpha = 0.01$, including radiative cooling. The temporal evolution of the two-dimensional temperature distribution

is shown in the pseudocolor maps of Fig. 3.7. At early times, the flow appears as a geometrically thick, hot configuration, with central temperatures of order $T \sim 10^9$ K after approximately one orbit. By around 3.5 orbits, the central temperature decreases to $\sim 10^8$ K, while the overall structure remains extended.

As the system evolves further, the morphology changes significantly: by ~ 5 orbits (at R_0), the flow develops a characteristic pinched or peanut-like structure, accompanied by the emergence of cold, high-density material in the equatorial region. At later times, around 7 orbits, a clear thinning is observed near $r = R_0$, indicating the formation of a geometrically thin disc with temperatures dropping to $\sim 10^4$ K, while a hot, low-density coronal component develops in the innermost region close to the black hole, reaching temperatures of $\sim 10^{11}$ K. The logarithmic temperature distribution is illustrated in Fig. 3.7, with temperature measured in Kelvin.

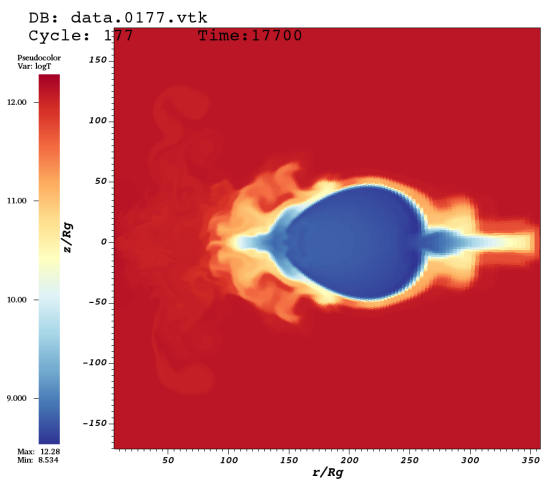
Since the cooling rate increases with density, the effective cooling time becomes sufficiently short in the high-density regime, enhancing the radiative efficiency of the flow, as also indicated in Fig. 3.10(d). This demonstrates that the initial peak density of the torus is sufficient to trigger bremsstrahlung cooling, which ultimately drives the transition from a hot, geometrically thick flow to a cold, thin disc.

To sustain a hot coronal region above the disc, thermal conduction is introduced in the upper layers, allowing material to evaporate from the disc into the corona [29]. In the present setup, the corona is maintained primarily through viscous heating, whereas in more general scenarios, magnetic dissipation and conductive processes can play a dominant role. Regardless of the heating mechanism, the corona is sustained through a quasi-dynamical and thermal balance [9].

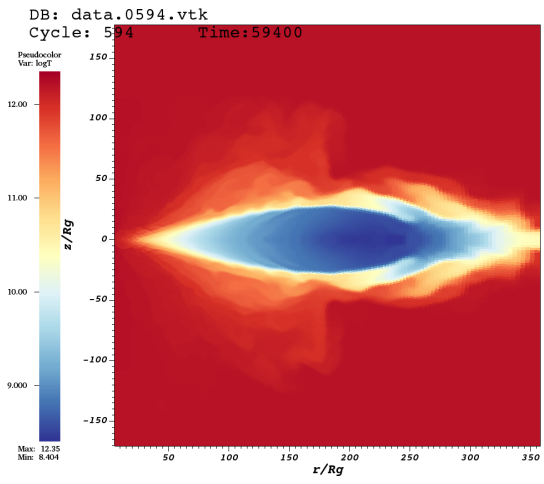
The development of the thin disc is further illustrated in Fig. 3.8, where the radial profile of the disc aspect ratio H/R is shown as a function of r/R_g. The ratio H/R provides a direct measure of the disc geometry. The scale height is estimated as $H \approx c_s/\Omega$, where the sound speed is evaluated at the mid-plane ($\theta = \pi/2$) using $c_s \approx \sqrt{P/\rho}$, and the angular velocity is approximated as $\Omega \approx \sqrt{GM/R^3}$.

At early times, the flow exhibits relatively large values of $H/R \gtrsim 0.1$, consistent with a thick disc structure. As evolution proceeds, this ratio decreases steadily, indicating the progressive formation of a geometrically thin disc. However, the innermost region remains relatively thick, while the thin disc ($H/R \lesssim 10^{-4}$) gradually propagates inward. Localised spikes in H/R arise from hot gas pockets near the equatorial plane, while the outermost regions also deviate from thin-disc behaviour due to long cooling times associated with low density.

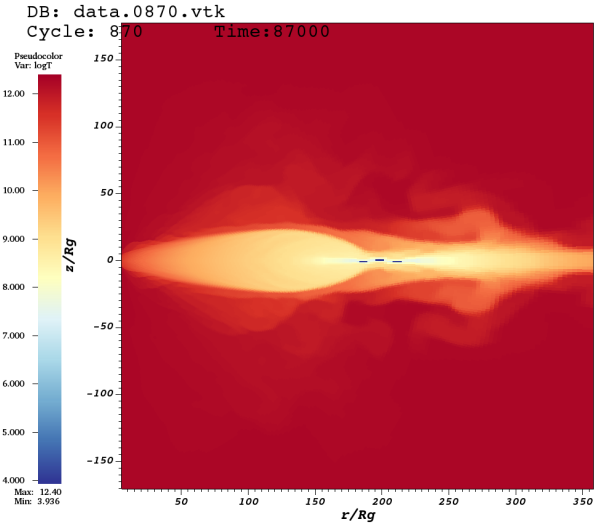
It is also important to note that the thin disc is characterised not only by low temperature but also by enhanced density, as material accumulates toward the mid-plane, reducing the cooling timescale. This is evident in Fig. 3.9, which compares early and late-time density distributions and shows an increase in density by approximately two orders of magnitude as the thin disc forms.



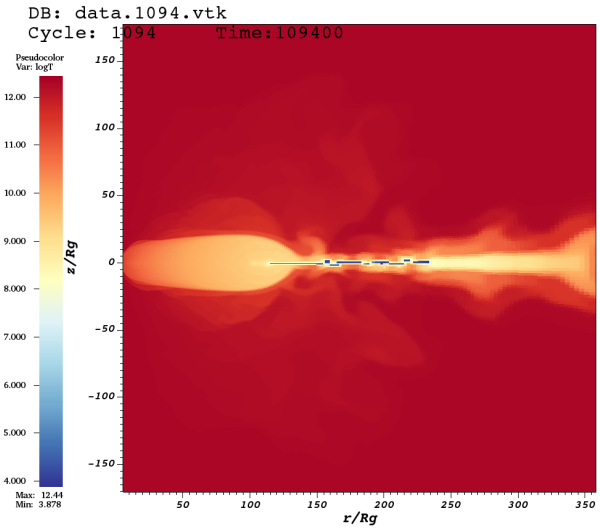
(a) 1 orbit



(b) 3.5 orbits



(c) 5 orbits



(d) 7 orbits

Figure 3.7: The evolution of pseudocolor Temperature plots with time. $\rho_0 = 10^{10}\, m_p$ g cm^{-3}. The resolution of the run is 512 x 512

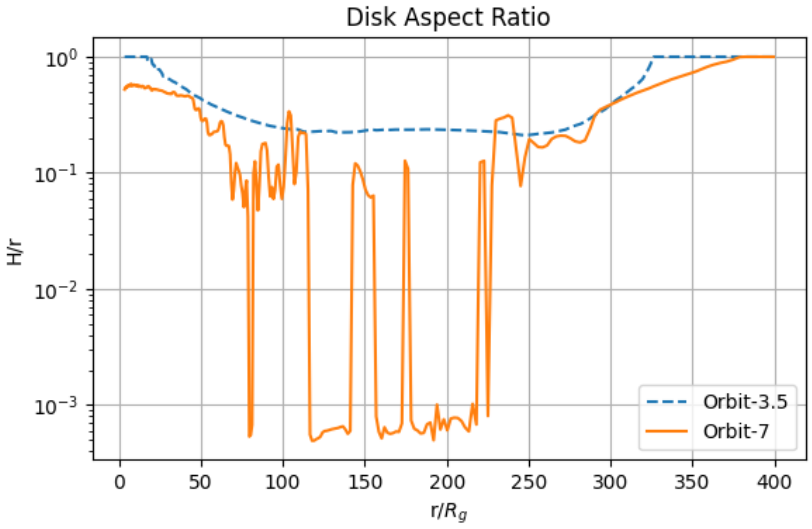
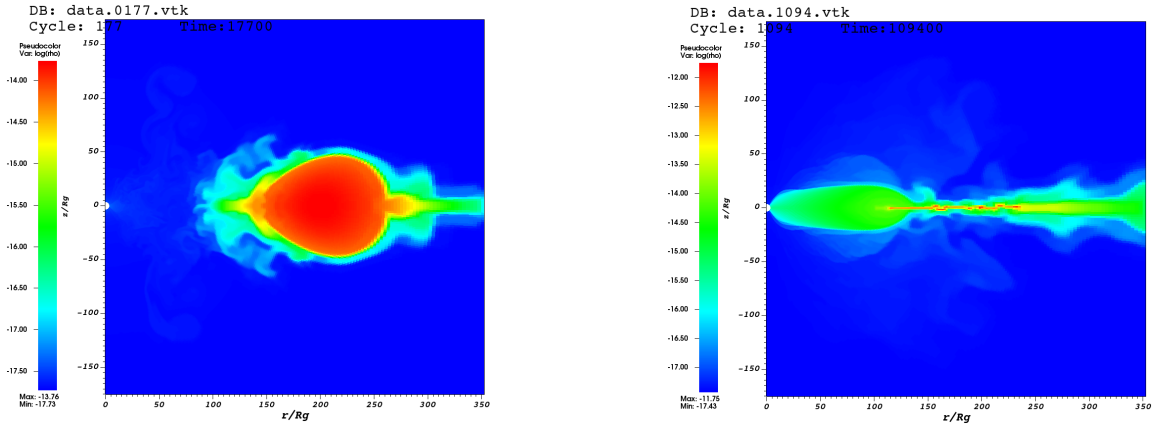


Figure 3.8: The variation of mid plane aspect ratio (H/R) with radius (r/R_g). The blue dotted lines and the orange line represent the plots corresponding to 3.5 orbits and 7 orbits respectively.



(a) 1 orbit **(b)** 7 orbits

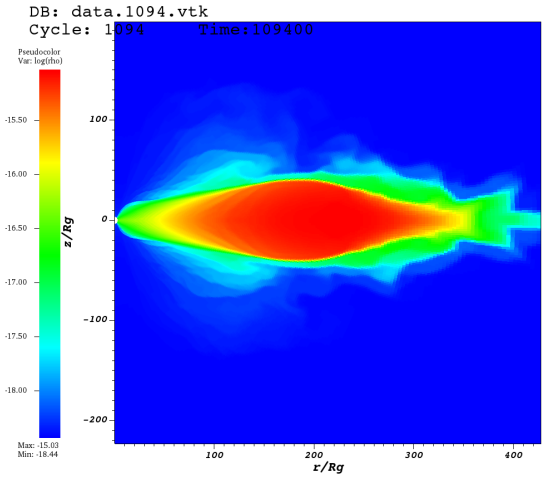
Figure 3.9: Pseudocolor density plot for cooling with $\rho_0 = 10^{10}\, m_p$ g cm^{-3}

Dependence on Initial Density

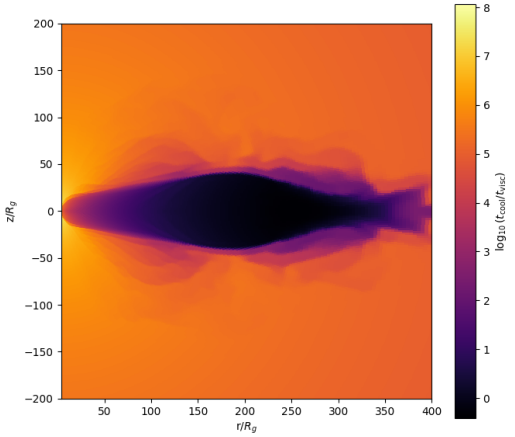
From Fig. 3.10, we identify the presence of a critical density above which condensation into a geometrically thin disc is triggered. The figure presents pseudocolor density maps for two simulations with $\rho_0 = 10^9\, m_p\,\mathrm{g\,cm^{-3}}$ and $\rho_0 = 10^{10}\, m_p\,\mathrm{g\,cm^{-3}}$, respectively (left panels), along with the corresponding distributions of the ratio $t_{\mathrm{cool}}/t_{\mathrm{visc}}$ (right panels). Both runs adopt the same viscosity parameter $\alpha = 0.01$, and therefore share identical viscous timescales; however, their cooling behaviour differs due to the differing initial densities.

For the lower-density case ($\rho_0 = 10^9\, m_p\,\mathrm{g\,cm^{-3}}$), the flow remains geometrically thick throughout the evolution, with $H/R \gtrsim 0.1$. In this regime, the accretion flow is best described as a low-density, hot coronal state that is radiatively inefficient.

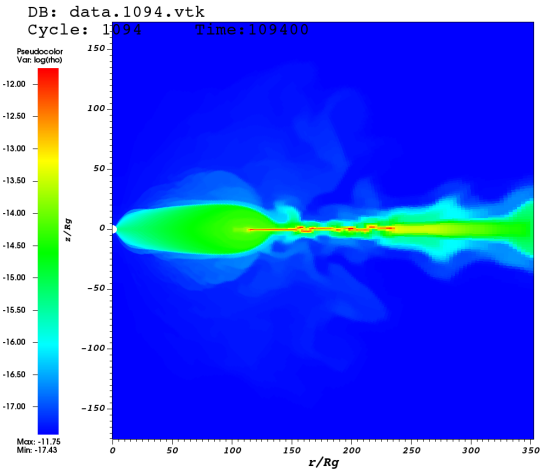
In contrast, increasing the initial density significantly alters the flow structure. The hot coronal region becomes confined to the inner radii, while a geometrically thin disc emerges with $H/R \lesssim 10^{-3}$. These results indicate that $\rho_0 = 10^{10}\, m_p\,\mathrm{g\,cm^{-3}}$ effectively represents a threshold density for the onset of efficient bremsstrahlung cooling and subsequent disc condensation [9].



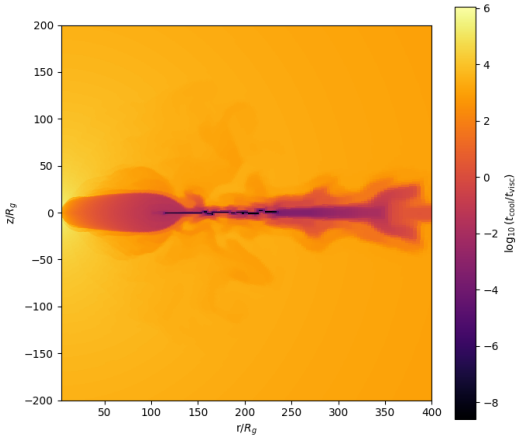
(a) $\rho_0 = 10^9\, m_p\,\mathrm{g\,cm^{-3}}$, 7 orbits



(b) $log_{10} t_{cool}/t_{visc}$,7 orbits



(c) $\rho_0 = 10^{10}\, m_p\,\mathrm{g\,cm^{-3}}$, 7 orbits



(d) $log_{10} t_{cool}/t_{visc}$,7 orbits

Figure 3.10: The evolution of pseudocolor Temperature plots with time. $\rho_0 = 10^{10}\, m_p\,\mathrm{g\,cm^{-3}}$. The resolution of the run is 512 x 512

The emergence of a geometrically thin disc is governed by the relative magnitudes of the cooling and viscous timescales, quantified by the ratio $t_{\rm cool}/t_{\rm visc}$. In Fig. 3.10(b), this ratio remains greater than unity throughout the computational domain, indicating that viscous heating dominates the energy balance. In this regime, the gas is accreted before it can efficiently radiate away its thermal energy, rendering radiative cooling dynamically ineffective.

However, the same figure also suggests that the ratio $t_{\rm cool}/t_{\rm visc}$ can fall below unity in the vicinity of the dense torus if its density is increased by an order of magnitude. This behaviour is confirmed in Fig. 3.10(d), where the ratio becomes significantly less than one over a substantial region, indicating that radiative cooling dominates over viscous heating.

In this cooling-dominated regime, the gas is able to lose its thermal energy prior to accretion, leading to condensation in the equatorial plane and the subsequent formation of a geometrically thin disc.

It should be noted that the computed values of $t_{\rm cool}/t_{\rm visc}$ are not fully realistic, as vertical radiative transport has been neglected in the present treatment.

3.1.3 State Transitions induced by cooling

A wide range of observational studies has established that black hole (BH) X-ray binaries display distinct spectral states [30, 5]. In these systems, the emission from the accretion flow alternates between a hard state, dominated by high-energy X-rays, and a soft state, in which thermal emission from the disc prevails. Transitions between these states typically occur over timescales of months to years.

Supermassive BHs in galactic centres are also expected to undergo analogous transitions, although on much longer timescales owing to the mass scaling of characteristic dynamical processes. The soft state is well described by the standard geometrically thin, optically thick Shakura–Sunyaev disc model, whereas the hard state is generally attributed to a hot, optically thin, radiatively inefficient accretion flow (RIAF).

Transitions from a RIAF to a thin disc are typically driven by an enhanced mass supply to the accretion flow. The resulting increase in density shortens the cooling timescale, eventually leading to conditions where $t_{\rm cool}/t_{\rm visc} < 1$. In the opposite direction, the depletion of material in a thin disc through accretion naturally causes the system to revert to a RIAF state, as the same ratio increases and exceeds unity in the inner regions.

Transition from a RIAF to thin disc

A RIAF can trasntion into a thin disc if its cooling time scale shortens in comaprison to its viscous timescales. A decrease in t_{cool} could be brought about by an increase in density as we saw in the previous section. However in this section we would not use ρ_0 as a proxy but will rather increase the density through an increase in the mass accretion rate. Such variability can arise from several physical mechanisms. In BH binaries, fluctuations in the mass accretion rate may be driven by variability in the stellar wind of the massive companion [31], instabilities developing near the Roche lobe [32], or intrinsic viscous instabilities within the accretion flow. The latter may result from thermal–viscous processes associated with strong opacity variations around temperatures of $\sim 10^4$ K [33].

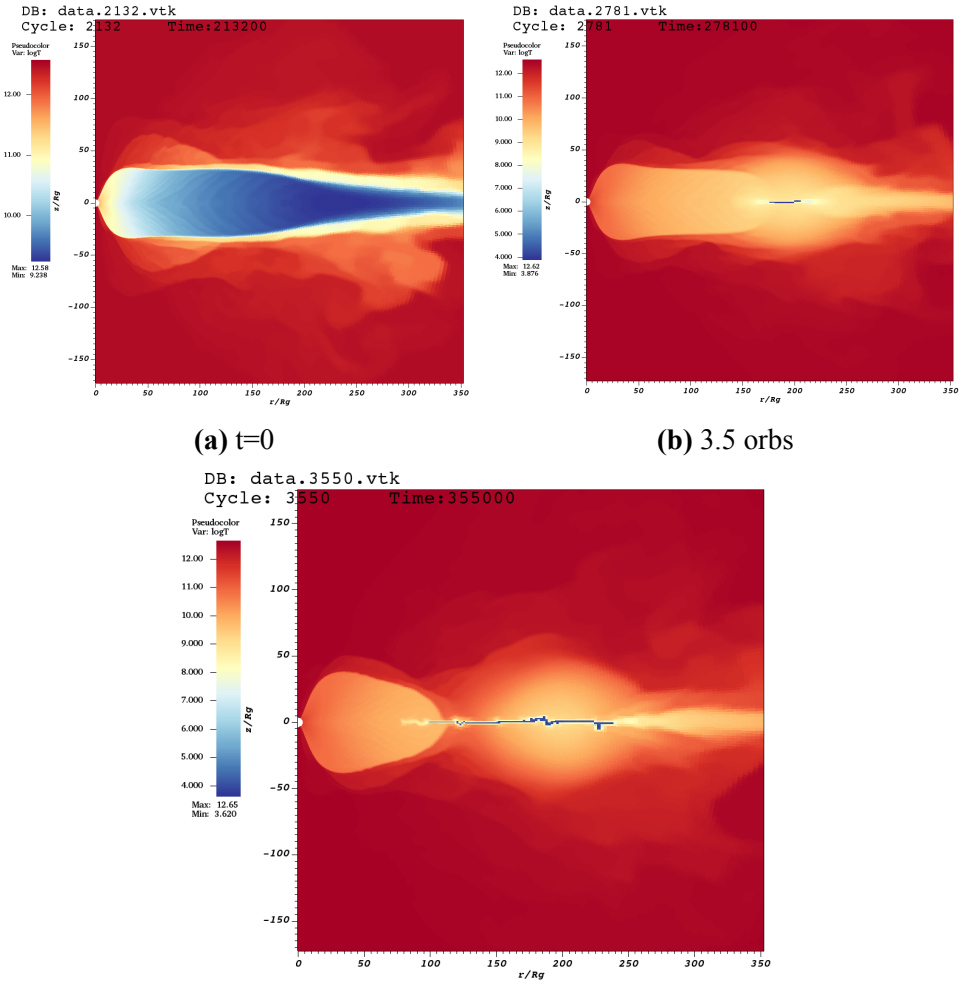
On larger scales, similar variability is also observed in active galactic nuclei (AGN). A notable example is the detection of a dense gas cloud infalling toward the accretion region of Sgr A*, the supermassive BH at the Galactic Centre [34]. This event is expected to temporarily enhance the mass accretion rate, leading to a significant increase in X-ray and broadband emis-

sion.

In our simulations the mass and density of RIAFs decrease with time as they get accreted. Equation 2.1 we used for our previous simulation didn't include any source term. In order to let our RIAF transition into a thin disc we need to add mass to our accretion flow. To mimic an increase in the mass accretion rate we include a source term to our continuity equation (Eqn 2.1) given by

$$\dot{\rho}(r,\theta) = 9\,\frac{\rho_0}{t_{\rm orb}}\,\exp\left(-\frac{(r\sin\theta - R_0)^2 + (r\cos\theta)^2}{(10R_g)^2}\right) \tag{3.2}$$

[9] Here, ρ_0 is the initial density normalization, and R_0 is the radius at which mass is injected, chosen to coincide with the centre of the initial dense torus at $200\,R_g$. The orbital time at R_0 is given by $t_{\rm orb} = \frac{2\pi}{\Omega_0}$. Mass is deposited over a characteristic scale of $10\,R_g$, beyond which the source function decreases rapidly. The injected mass is assumed to carry the local velocity and internal energy density of the flow[9].



(a) t=0 **(b)** 3.5 orbs

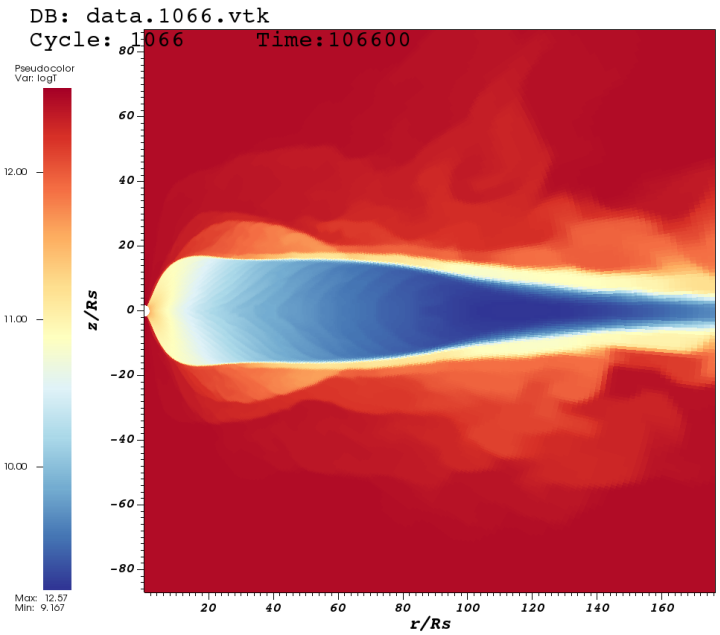
(c) 8 orbs

Figure 3.11: Transition from a geometrically thick RIAF state dominated by viscous heating into a geometrically thin cold disc induced by addition of mass. The grid reasolution is 512 x 512

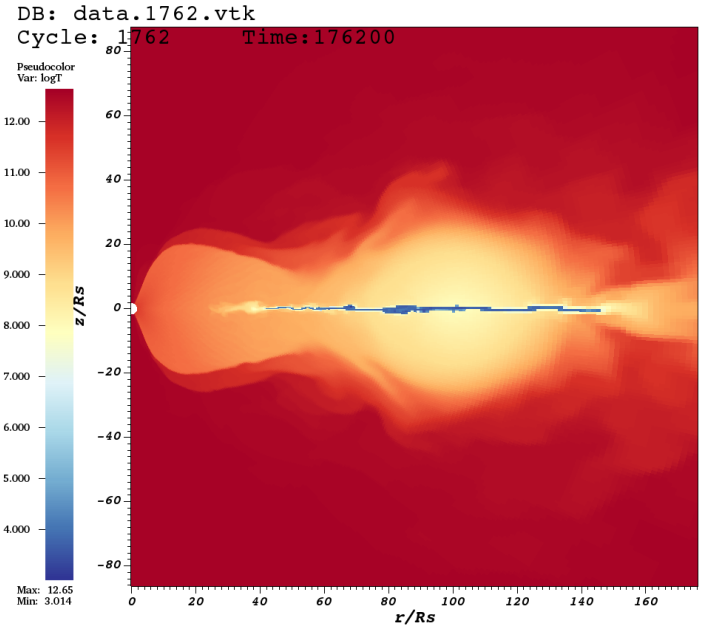
The initial condition of our run is the last stage of evolving a low density torus with $\rho_0 =$

$10^9\ m_p$ g cm^{-3} as shown in Fig 3.10(c) without cooling for about 10 orbits. For comparison it is very similar to our initial run with $\rho_0 = 10^6\ m_p$ g cm^{-3} 3.1(e) at around 10 orbits as pure RIAF runs without cooling are independent of density normalization. The mass is added to local temperatures of $10^9 - 10^{10}$ at $r = R_0$ as shown in Fig 3.11(a). The addition of mass can be clearly seen as the formation of a bulge around $r = R_0$ in Fig 3.11(b). Since the addition of mass in continuous it eventually leads to an increase in density and shortens the cooling timescale allowing for the formation of a cold thin disc ($T \sim 10^4 K$). As expected the thin discs starts forming at $r = R_0$ (3.11(b))point as the mass addition is concentrated around it. After 3.5 orbits the ratio of t_{cool}/t_{visc} becomes much lesser than 0 thus onsetting the thin disc. As we continue to run our simulation the thin disc extends closer to the black hole surrounded by a low density hot corona ($T \sim 10^{10-11} K$) as seen in Fig 3.11(c)

A further insight can be derived by looking at Fig 3.13 where at the initial stage the ratio of t_{cool}/t_{visc} is greater than 1 everywhere suggesting a flow dominated by viscous heating which transitions into a flow dominated by cooling as the ratio of t_{cool}/t_{visc} drops significantly ($\ll 1$) leading to the formation of a thin disc.



(a) t=0

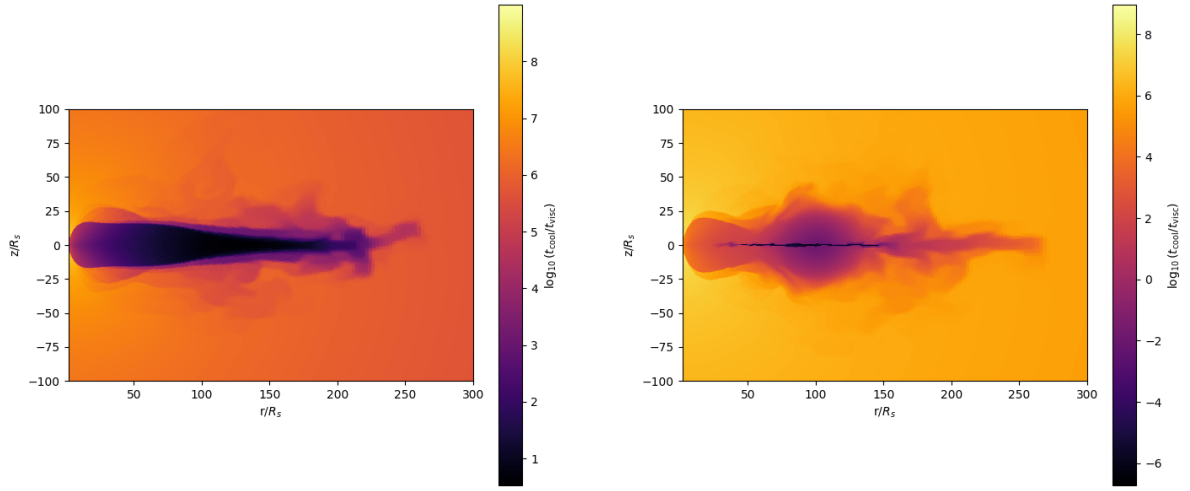


(b) 8 orbs

Figure 3.12: High resolution run showing the transition from a hot RIAF state to a cold thin disc (around 8 orbits).

Our runs suffers from the problem of low resolution. A direct consequence of which is, our thin disc does not remain stable for longer periods of time. With time as more gas condenses onto the mid plane the mid plane aspect ratio (H/R) of the gas keeps decreasing which makes it harder to resolve. With values of $H/R < 10^{-4}$ eventually our grid becomes incapable of capturing the thin disc which leads to the diappearence of the disc which is instead replaced by hot gas. The spikes we see in 3.8 appears due to the same reason. We try to atleast run one high resolution run to investigate how it will improve our simulation. We increase the resolution by reducing our grid size to $1.75R_s - 400R_s$ where R_s is the Schwarzschild radius. This keeps

the physical distances exactly similar to our previous runs ($R_s = 2R_g$) all the while giving us a better resolution due to the decrease in grid size.
We perform the exact same run with $\rho_0 = 10^9\, m_p$ g cm^{-3} and simulating a RIAF. After which we start adding mass around $100R_s$ and as seen in Fig 3.12 we obtain a thin disc that is much more prominent,longer (1 unit in this run equals to 2 units in the previous runs) and even extends much closer to the black hole.



(a) t=0 **(b)** 8 orbs

Figure 3.13: t_{cool}/t_{visc} ratio for high resolution run of state transition induced by an increase in mass accretion rate

With an increase in our resolution we even observe a better H/R diagram as shown in 3.14 . The plots shows values of $H/R \sim 10^{-4}$ over extended lengths suggesting our run has captured the thin disc better this time.

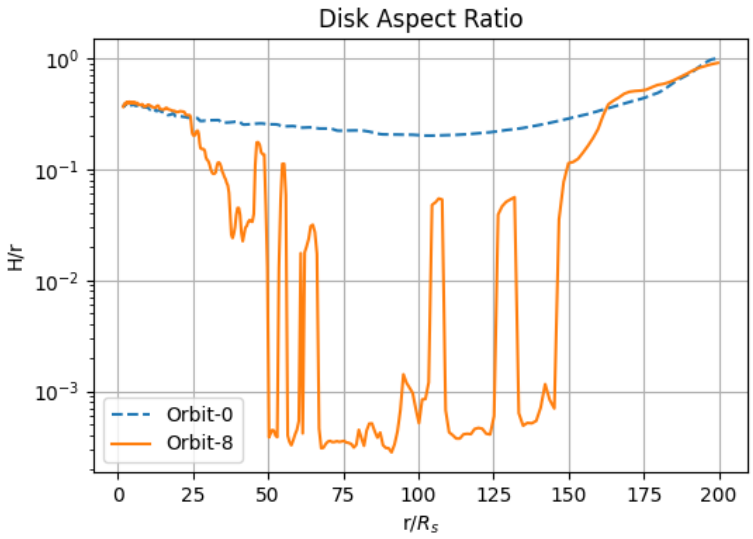


Figure 3.14: The variation of mid plane aspect ratio (H/R) with radius (r/R_s). The blue dotted lines and the orange lines represent the plots corresponding to 0 and 8 orbits respectively.

Chapter 4

Future Work

Through our entire work we came to a few conclusions regarding the mechanism of an accretion disc around a black hole and the physical processes behind it. State transitions are in general a widely observed phenomena [5] and constant work is being put to model and understand the various phenomena surrounding it. Through our work we used our limited time and resources to understand a part of its mechanism. However we are still far from modelling an accretion flow with realistic parameters and physical parameters. There are some improvements and work that can be extended from our work in the future.

- The thin disc are often very hard to resolve with ($H/R \ll 1$) as the gas continues to settle around the mid-plane in the long run the disc becomes too thin to resolve in one of our grids with a grid size of 512^2. As a result of which the thin disc slowly starts disappearing and is replaced by hot gas which is a reason behind the spiked in our H/R diagrams. In the future a high resolution run of 1024^2 could solve this problems and keep a geometrically thin cold disc stable in the long run

- Thermal conductivity plays a significant role in maintaining the thermal equilibrium that exists between the corona and the thin disc[29]. In our runs we only rely on viscous heating and optically thin radiative cooling. However in reality the conductivity leads to the evaporation of the cold thin disc into the corona via conduction ans as it continues the corona reaches a critical density to finally have a value of $t_{cool}/t_{visc} \ll 1/$ and again settle in the mid plane. In the future runs thermal conductivity could be included to get an accurate estimate of cooling and viscous timescales

- We have already concluded that an increase in the mass accretion rate can lead an RIAF (Hard state) to transition into a cold thin disc (Soft State). However to mimic an increase increase in the mass accretion rate we have used an external function as the source. However if we wish to enquire into the true mechanics of the transitions actually observed, we should look into some inherent physical processes like Thermal Viscous Instability/variations in stellar winds of the companion star or instabilities regarding the Roche lobe that arises from the very physics of an accretion flow. Rather than providing an external mass function by incorporating a Disc Instabilty Model (DIM) ([35],[36],[37]) or other instability model [31], in our work we can explain and understabd state transitions even more fundamentally.

References

[1] Bradley W. Carroll and Dale A. Ostlie. *An Introduction to Modern Astrophysics*. Pearson Addison-Wesley, San Francisco, 2 edition, 2007.

[2] Juhan Frank, Andrew R. King, and Derek J. Raine. *Accretion Power in Astrophysics*. Cambridge University Press, Cambridge, UK, 3rd edition, 2002. ISBN 0521620538, 9781139164245. doi: 10.1017/CBO9781139164245.

[3] S. A. Balbus and J. F. Hawley. A powerful local shear instability in weakly magnetized disks. i. linear analysis. *The Astrophysical Journal*, 329:678–692, 1988. doi: 10.1086/166404.

[4] B. L. Webster and P. Murdin. Cygnus x-1—a spectroscopic binary with a heavy companion? *Nature*, 235:37–38, 1972. doi: 10.1038/235037a0.

[5] Ronald A. Remillard and Jeffrey E. McClintock. X-ray properties of black-hole binaries. *Annual Review of Astronomy and Astrophysics*, 44(1):49–92, 2006. doi: 10.1146/annurev.astro.44.051905.092532. URL https://doi.org/10.1146/annurev.astro.44.051905.092532.

[6] H. Tananbaum, E. Gursky, R. Kellogg, R. Giacconi, and E. Schreier. Observation of a correlated x-ray transition in cygnus x-1. *The Astrophysical Journal Letters*, 177:L5–L8, 1972. doi: 10.1086/181698.

[7] S. Ichimaru. Bimodal behavior of accretion disks — theory and application to cygnus x-1 transitions. *Astrophysical Journal*, 214:840, 1977.

[8] N. I. Shakura and R. A. Sunyaev. Black holes in binary systems. observational appearance. *Astronomy & Astrophysics*, 24:337, 1973.

[9] U. Das and P. Sharma. Radiatively inefficient accretion flow simulations with cooling. *Monthly Notices of the Royal Astronomical Society*, 435(3):2431–2444, 2013. doi: 10.1093/mnras/stt1452.

[10] Università di Torino. Pluto code — physics department, university of torino. URL https://plutocode.ph.unito.it/.

[11] S. E. Woosley, A. Heger, and T. A. Weaver. The evolution and explosion of massive stars. *Reviews of Modern Physics*, 74:1015–1071, 2002. doi: 10.1103/RevModPhys.74.1015.

[12] M. J. Rees, M. C. Begelman, R. D. Blandford, and E. S. Phinney. Ion-supported tori and the origin of radio jets. *Nature*, 295:17–21, 1982. doi: 10.1038/295017a0.

[13] J. M. Stone, J. E. Pringle, and M. C. Begelman. Hydrodynamical non-radiative accretion flows in two dimensions. *Monthly Notices of the Royal Astronomical Society*, 310:1002, 1999.

[14] I. V. Igumenshchev, R. Narayan, and M. A. Abramowicz. Three-dimensional magnetohydrodynamic simulations of radiatively inefficient accretion flows. *The Astrophysical Journal*, 592:1042–1059, 2003. doi: 10.1086/375769.

[15] K. Beckwith, J. F. Hawley, and J. H. Krolik. The influence of magnetic field geometry on the evolution of black hole accretion flows: Similar disks, drastically different jets. *The Astrophysical Journal*, 678:1180–1199, 2008. doi: 10.1086/533492.

[16] R. F. Penna, J. C. McKinney, R. Narayan, A. Tchekhovskoy, R. Shafee, and J. E. McClintock. Simulations of magnetized discs around black holes: effects of black hole spin, disc thickness and magnetic field geometry. *Monthly Notices of the Royal Astronomical Society*, 408:752–782, 2010. doi: 10.1111/j.1365-2966.2010.17170.x.

[17] K. Ohsuga, S. Mineshige, M. Mori, and Y. Kato. Global radiation-magnetohydrodynamic simulations of supercritical accretion flows. *Publications of the Astronomical Society of Japan*, 61:L7–L11, 2009. doi: 10.1093/pasj/61.3.L7.

[18] K. Ohsuga and S. Mineshige. Global radiation-magnetohydrodynamic simulations of black hole accretion flow: Slim disks with outflows. *The Astrophysical Journal*, 736: 1–19, 2011. doi: 10.1088/0004-637X/736/1/1.

[19] J. C. B. Papaloizou and J. E. Pringle. The dynamical stability of differentially rotating discs - i. the local axisymmetric case. *Monthly Notices of the Royal Astronomical Society*, 208:721, 1984.

[20] A. M. Ghez, S. Salim, N. N. Weinberg, J. R. Lu, T. Do, J. K. Dunn, K. Matthews, M. R. Morris, S. Yelda, E. E. Becklin, T. Kremenek, M. Milosavljevic, and J. Naiman. Measuring distance and properties of the milky way's central supermassive black hole with stellar orbits. *Astrophysical Journal*, 689:1044, 2008.

[21] Axel Brandenburg, Åke Nordlund, Robert F. Stein, and Uriel Torkelsson. Dynamo-generated turbulence and large-scale magnetic fields in a keplerian shear flow. *The Astrophysical Journal*, 446:741–754, 1995. doi: 10.1086/175831.

[22] John F. Hawley, Charles F. Gammie, and Steven A. Balbus. Local three-dimensional magnetohydrodynamic simulations of accretion disks. *The Astrophysical Journal*, 440: 742–763, 1995. doi: 10.1086/175311.

[23] Prateek Sharma, Ian J. Parrish, and Eliot Quataert. Thermal instability and the feedback regulation of hot halos in clusters, groups, and galaxies. *The Astrophysical Journal*, 720 (1):652–665, 2010. doi: 10.1088/0004-637X/720/1/652.

[24] Ralph S. Sutherland and Michael A. Dopita. Cooling functions for low-density astrophysical plasmas. *The Astrophysical Journal Supplement Series*, 88:253–327, 1993. doi: 10.1086/191823.

[25] Tsvi Piran. On dynamical time scales and stability of accretion disks. *The Astrophysical Journal*, 221:652–660, 1978. doi: 10.1086/156071.

[26] Prateek Sharma, Michael McCourt, Eliot Quataert, and Ian J. Parrish. Thermal instability and multiphase structure in simulated cooling flows. *Monthly Notices of the Royal Astronomical Society*, 420:3174–3194, 2012. doi: 10.1111/j.1365-2966.2011.20398.x.

[27] Daniel Proga and Mitchell C. Begelman. Accretion of low angular momentum material onto black holes: Two-dimensional hydrodynamical inviscid case. *The Astrophysical Journal*, 592(2):767–781, 2003. doi: 10.1086/375772.

[28] F. K. Baganoff, Y. Maeda, M. Morris, M. W. Bautz, W. N. Brandt, W. Cui, J. P. Doty, E. D. Feigelson, G. P. Garmire, S. H. Pravdo, G. R. Ricker, and L. K. Townsley. Chandra x-ray spectroscopic imaging of sagittarius a* and the central parsec of the galaxy. *The Astrophysical Journal*, 591(2):891–915, 2003. doi: 10.1086/375145.

[29] F. Meyer and E. Meyer-Hofmeister. On the evaporation of accretion disks. *Astronomy and Astrophysics*, 288:175–182, 1994.

[30] R. P. Fender, T. M. Belloni, and E. Gallo. Towards a unified model for black hole x-ray binary jets. *Monthly Notices of the Royal Astronomical Society*, 355:1105–1118, 2004. doi: 10.1111/j.1365-2966.2004.08384.x.

[31] T. Eversberg, S. Lépine, and A. F. J. Moffat. Outmoving clumps in the wind of the hot o supergiant ζ puppis. *The Astrophysical Journal*, 494:799–805, 1998. doi: 10.1086/305218.

[32] K. Sawada, T. Matsuda, and I. Hachisu. Spiral shocks on accretion disks in close binary systems. *Monthly Notices of the Royal Astronomical Society*, 219:75–88, 1986. doi: 10.1093/mnras/219.1.75.

[33] F. Meyer and E. Meyer-Hofmeister. On the evaporation of accretion disks. ii. *Astronomy and Astrophysics*, 104:L10–L12, 1981.

[34] S. Gillessen, R. Genzel, T. K. Fritz, E. Quataert, C. Alig, A. Burkert, J. Cuadra, F. Eisenhauer, O. Pfuhl, T. Ott, A. Ballone, and M. Schartmann. A gas cloud on its way towards the supermassive black hole at the galactic centre. *Nature*, 481:51–54, 2012. doi: 10.1038/nature10652.

[35] Guillaume Dubus, Jean-Marie Hameury, and Jean-Pierre Lasota. The disc instability model for x-ray transients: Evidence for truncation and irradiation. *Astronomy & Astrophysics*, 373:251–271, 2001. doi: 10.1051/0004-6361:20010632.

[36] Jean-Marie Hameury. A review of the disc instability model for dwarf novae, soft x-ray transients and related objects. *Advances in Astronomy*, 2019.

[37] Jean-Pierre Lasota. The disc instability model of dwarf novae and low-mass x-ray binary transients. *New Astronomy Reviews*, 45(7):449–508, 2001. doi: 10.1016/S1387-6473(01)00112-9.